

End-Capping Fluorination of Vinylene-Linked Covalent Organic Frameworks for Photocatalytic Hydrogen Peroxide Production

Anqi Chen,^a Yi Jian,^b Qiujian Xie,^a Wen Li,^a Chunyue Pan,^a Guipeng Yu,^a Shuai Gu^{*a} and Juntao Tang^{*a}

^a *Hunan Key Laboratory of Micro & Nano Materials Interface Science, College of Chemistry and Chemical Engineering, Central South University, Changsha 410083, P. R. China. E-mail: reynardtang@csu.edu.cn*

^b *Geological Experiment and Testing Center of Hunan Province, Changsha 410007, P. R. China.*

Table of Contents

1. Materials and methods	3
2. Synthetic procedures	4
3. Photocatalytic performance evaluations	9
4. Results and discussion	11
5. NMR spectra of monomers	34
6. Reference	36

Supporting Information

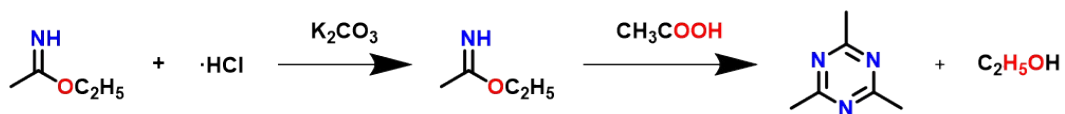
Section 1. Materials and methods

2,4,6-trimethyl-1,3,5-triazine (TMT) was synthesized according to the reported procedures¹. The monomers, including Terephthalaldehyde (TA) and 2,3,5,6-Tetrafluoroterephthalaldehyde (TFTA), were commercially available and directly used. Materials and solvents in this work, were purchased in high purity from commercial sources and used without further purification.

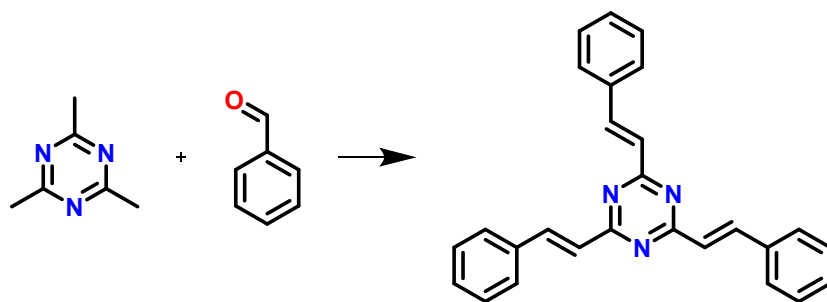
Characterizations

The obtained samples were prepared by dispersing in KBr powder and the corresponding FT-IR spectra were measured in the 4000-400 cm^{-1} region (VARIAN 1000 FT-IR spectrometer). Powder X-ray diffraction (PXRD) data was collected on a RINT-2000 instrument (Rigaku Corporation) using a $\text{CuK}\alpha$ anode ($\lambda = 0.154178 \text{ \AA}$) radiation operating at 20 kV and 20 mA. All the samples were recorded in the 2θ range of 3-30 degrees with a step size of 0.02 degrees and an exposure time of 0.06 seconds per step. PXRD simulations were performed using the Reflex module in the Materials Studio 6.0. Surface areas were measured by nitrogen adsorption and desorption at 77 K using Micromeritics ASAP 2020M. All samples were degassed at 100 °C for 12 hours before the gas adsorption experiment. And pore size distributions were calculated using the non-local density functional theory (NLDFT) method in the Quadrawin software. SEM measurements were performed on a FEI Sirion-200 field emission scanning electron microscope. ^1H and ^{13}C NMR spectra were measured with the deuterated solvents (CDCl_3 and DMSO-d_6) and employed the tetramethyl silane (TMS) as an internal standard (Bruker AM-400 MHz NMR spectrometer). The UV-Vis absorption spectra of the powders in the solid state were obtained on a scan UV-Vis spectrophotometer (U-4100 spectrometer). The electrochemical impedance spectra (EIS) was performed on an electrochemical workstation at room temperature in the dark (CHI760E). The photocurrent of the polymer was performed on a VersaSTAT 3 electrochemical workstation under irradiation of 300 W Xe lamp. The density functional theory (DFT) calculations were applied to optimize the geometry of monomers and oligomers (B3LYP functional, and 6-311G(d) basis set). The molecular configuration optimization and Gibbs free energy was carried out by DFT calculations (Gaussian 09 software package and Gauss View visualization program).

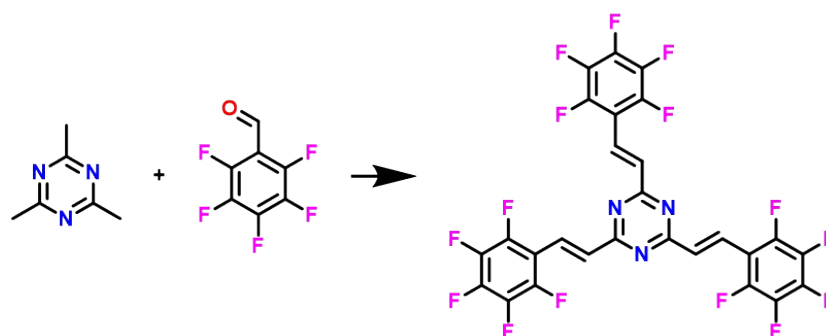
Section 2. Synthetic procedures



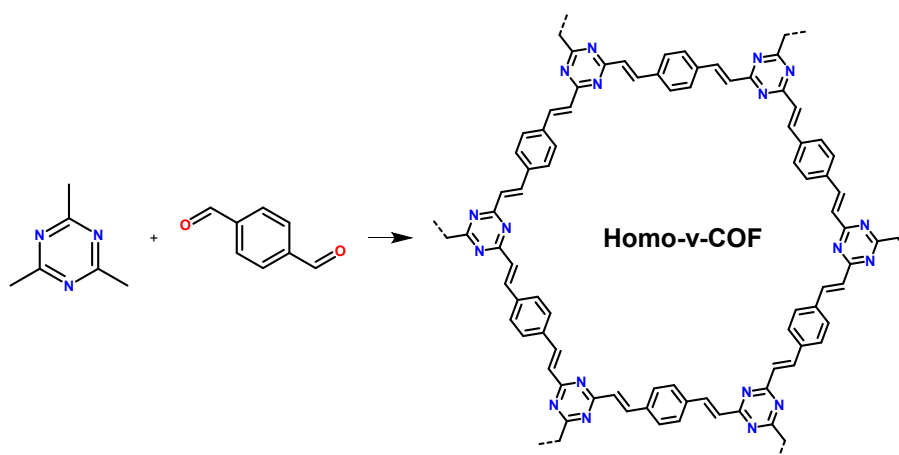
Synthesis of 2,4,6-trimethyl-1,3,5-triazine (TMT): The synthesis of 2,4,6-trimethyl-1,3,5-triazine monomer was mainly obtained by referring to the experimental method that has been reported before.¹ Potassium carbonate (28.70 g, 0.20 mol) was dissolved in 100 mL of water, and 35 mL of dichloromethane was added with stirring; ethyl acetimidate hydrochloride (17.30 g, 0.20 mol) was weighed and slowly added to the above solution, and stirred rapidly at room temperature for 10 min. The organic phase was then extracted and separated, and the organic phase was dried with anhydrous potassium carbonate after the extraction was repeated twice by adding dichloromethane. The organic phase was dried with anhydrous potassium carbonate. The filtrate was collected by filtration and distilled to remove the low-boiling-point (<60 °C) fraction, and a highly concentrated ethyl acetimidate liquid in light yellow was obtained. Glacial acetic acid (0.70 mL, 12 mmol) was slowly added dropwise to the liquid under stirring in an ice bath at 0 °C and stirred for 5 min, after which the ice bath was removed and the reaction was carried out at room temperature for 24 h. After the reaction was complete, the solution was distilled again to remove the fractions below the boiling point of 90 °C. The solution was diluted with dichloromethane and potassium carbonate was added to remove the unreacted acetic acid. The organic phase was separated and distilled at 120 °C to collect the crude product of 2,4,6-trimethyl-1,3,5-triazine, which was finally recrystallized using ether to obtain the pure white crystal product (1.82 g, 22 %).



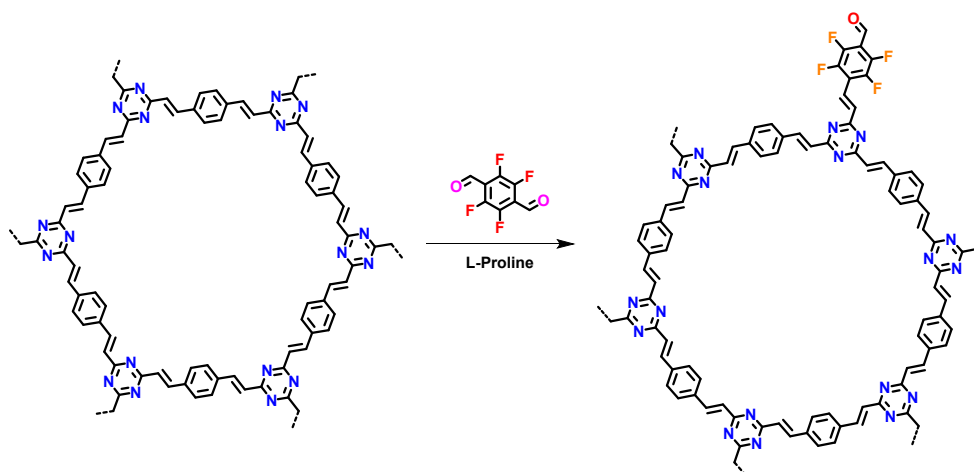
Synthesis of model compound 1: The model product was prepared following a previously reported literature synthesis method.² The procedure was conducted as follows: 2,4,6-trimethyl-1,3,5-triazine (TMT) (310 mg, 2.52 mmol), benzaldehyde (1061.2 mg, 10 mmol), and KOH (561 mg, 10 mmol) were added to 50 mL of CH₃OH and heated to 80 °C. The reaction was carried out under a nitrogen atmosphere for 24 hours. Upon completion, the crude product was extracted into dichloromethane. After solvent removal, the solid residue was collected and further purified through recrystallization in a mixed solvent system. Recrystallization using a mixed dichloromethane/CH₃OH solution yielded the pure model compound as a white solid. The yield was 82% (802.0 mg).



Synthesis of model compound 2: The model compound 2 was synthesized following a modified literature procedure with optimized reaction conditions.³ In a typical synthesis, 2,4,6-trimethyl-1,3,5-triazine (TMT, 6.0 mg, 0.049 mmol) and 2,3,4,5,6-pentafluorobenzaldehyde (0.15 mmol) were precisely weighed into a 10 mL ampoule tube. Subsequently, a mixed solvent system consisting of mesitylene (0.45 mL), 1,4-dioxane (0.45 mL), acetonitrile (0.025 mL), and trifluoroacetic acid (0.2 mL) was sequentially added to the reaction vessel. The ampoule was subjected to three freeze-pump-thaw cycles using liquid nitrogen to ensure complete removal of oxygen before flame-sealing under vacuum. The sealed ampoule was then placed in a preheated oven at 150 °C for 72 h to facilitate the reaction. After cooling to room temperature, the ampoule was carefully opened, and the resulting mixture was filtered through funnel. The collected solid was thoroughly washed with anhydrous ethanol (3×10 mL) to remove residual reactants and byproducts. The washed product was then dried under reduced pressure at 60 °C for 12 h. Further purification was achieved through Soxhlet extraction with tetrahydrofuran for 24 h, followed by final vacuum drying to yield the pure model compound.



Synthesis of Homo-v-COF: The synthesis of the Homo-v-COF primarily followed a methodology previously reported in the literature.² Specifically, 2,4,6-trimethyl-1,3,5-triazine (61.58 mg, 0.50 mmol), terephthalaldehyde (100.60 mg, 0.75 mmol), and KOH (84.15 mg, 1.50 mmol) were added to a 25 mL autoclave reactor. To this mixture, anhydrous n-butanol (7 mL) and 1,2-dichlorobenzene (3 mL) were added, and the reactor was sonicated for 10 minutes. After sonication, the reactor was continuously purged with nitrogen for 30 minutes to ensure complete removal of oxygen. The reactor was then sealed, and the reaction was carried out at 120 °C for 3 days. Upon completion, the reactor was cooled to room temperature, and the crude product was collected by filtration. The crude product was washed three times with methanol, distilled water, tetrahydrofuran, and dichloromethane, respectively. Subsequently, the crude product was solubilized in methanol for 24 hours and then dried under vacuum at 65 °C for 12 hours. This procedure yielded a fluffy bright yellow solid powder of Homo-v-COF (120.30 mg, 89%).

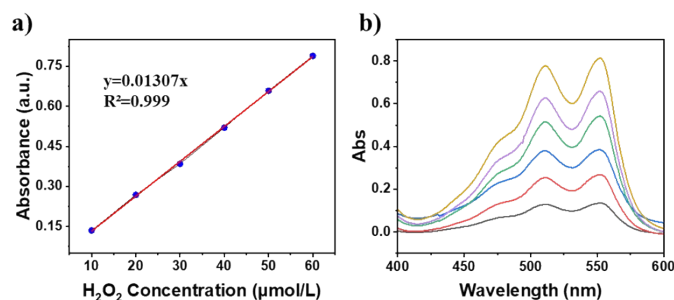


Synthesis of Post-v-COF-Fx: Homo-v-COF (44.00 mg, 0.24 mmol), L-proline (27.60 mg, 0.24 mmol), 2,3,5,6-tetrafluoro-p-diphenylaldehyde (12.57 mg, 0.06 mmol; 25.14 mg, 0.12 mmol; 37.72 mg, 0.18 mmol; 50.29 mg, 0.24 mmol) were added to the ampoule. Anhydrous n-butanol (1.40 mL) and anhydrous o-dichlorobenzene (0.60 mL) were then introduced into the ampoule. The mixture underwent three cycles of freezing, evacuating, nitrogen filling, and thawing. After the final freezing step, the ampoule was sealed under vacuum and placed in an oven at 120 °C for 3 days. Upon completion of the reaction, the polymer was cooled to room temperature, collected by filtration, and washed sequentially with methanol, distilled water, tetrahydrofuran, and dichloromethane (three times). The crude product was then soaked in methanol for 24 hours. Finally, the products were dried under vacuum at 65 °C for 12 hours, yielding a series of polymers with varying fluorine content (Post-v-COF-F1, Post-v-COF-F2, Post-v-COF-F3, and Post-v-COF-F4).

Section 3. Photocatalytic performance evaluations

Photocatalytic H₂O₂ production: 5 mg photocatalysts (Homo-v-COF and Post-v-COF-Fx) were dispersed into a quartz tube with 10 mL water, the suspension was dispersed for 15 minutes by ultrasonication and bubbled with oxygen for 30 minutes to achieve adsorption-desorption equilibrium. 40 W blue LED lamp was used as the light source and oxygen balls were used to bubble into the quartz tube continuously, and circulating cooling water was passed in to keep the room temperature. The sample after the reaction was taken by syringe at regular intervals to evaluate the performance of H₂O₂, and then stored in a light-proof place as the sample to be tested. N, N-diethyl-p-phenylenediamine sulfate (DPD) was used for the detection of H₂O₂ concentration. The generated H₂O₂ was added dropwise in PBS buffer to keep the solution neutral and prevent the decomposition of H₂O₂ due to heat as well as pH environment. Under the action of horseradish peroxidase (POD), H₂O₂ decomposes to produce ·OH, which subsequently reacts with DPD, converting the colorless DPD to pink DPD⁺. The yield of H₂O₂ was obtained by a liquid UV test of this process.⁴

H₂O₂ detection methods: A DPD reagent was prepared by dissolving 100 mg of DPD in 10 mL of a 0.05 mol L⁻¹ H₂SO₄ solution. Similarly, a POD reagent was prepared by dissolving 10 mg of horseradish peroxidase in 10 mL of ultrapure water. Additionally, 4.8 g of PBS powder (primarily composed of potassium dihydrogen phosphate) was dissolved in 500 mL of ultrapure water, and the solution was quantitatively prepared using a volumetric flask. To establish the calibration curve, 20 μL of DPD solution and 20 μL of POD solution were added to 1 mL of a PBS solution containing a known concentration of H₂O₂ (diluted 10-fold with PBS buffer). The mixture was then analyzed using a UV-vis spectrophotometer. By leveraging the linear relationship between the signal intensity and the concentration of DPD⁺, the H₂O₂ concentrations in the samples were determined (as below).



Standard curve of H₂O₂: (a) Standard curve; (b) Time-dependent UV spectra.

Mechanism of Photocatalytic H₂O₂ Production: Control experiments confirmed the critical roles of oxygen, light irradiation, electrons, and superoxide radicals in the photocatalytic H₂O₂ generation process. Electron paramagnetic resonance tests verified the existence of superoxide radical intermediates, suggesting that H₂O₂ is primarily produced via the oxygen reduction pathway. Rotating disk electrode measurements supported the two-step single-electron oxygen reduction mechanism. Additionally, in situ infrared spectroscopy confirmed the formation of superoxide radicals and H₂O₂, while density functional theory calculations revealed that the fluorinated benzene ring acts as an oxygen adsorption site, thereby enhancing the photocatalytic H₂O₂ production.

Determination of Electron transfer number: The electron transfer number for oxygen reduction reaction was performed on a rotating disk electrode in O₂ saturated seawater with different rotating speed. The average number of electrons (n) can be estimated by linear regression of the plots using the following equations:

$$j^{-1} = j_k^{-1} + j_d^{-1}$$
$$j_d = 0.620 n F C_0 D^{2/3} \omega^{1/2} \nu^{-1/6}$$

where j is the current density, j_k is the kinetic current density, ω is the rotating speed (rad s⁻¹), F is the Faraday constant (96485 C mol⁻¹), ν is the kinetic viscosity of water (0.01 cm² s⁻¹), C₀ is the bulk concentration of O₂ in water (1.2 × 10⁻³ mol cm⁻³), and D is the diffusion coefficient of O₂ (1.9 × 10⁻⁵ cm² s⁻¹)

Spin trapping-EPR tests: The measurements were recorded using a Bruker EMX plus model spectrometer operating at the X-band frequency (9.4 GHz). 5,5-dimethyl-1-pyrroline N-oxide (DMPO) were used as a spin-trapping reagents to detect •O₂⁻. A Xe lamp (λ > 420 nm) was used as the light source. The dispersion was purged with O₂ or Ar gas for 5 min before light irradiation.

In situ DRIFT spectra: To further investigate the activation process of the oxygen reduction reaction, in situ DRIFTS tests were conducted on a Tensor II FT-IR spectrometer (Bruker). Prior to testing, the reaction chamber was purged with high-purity He gas for 60 minutes. Subsequently, a mixed gas containing saturated water vapor and O₂ was introduced into the reaction chamber at a flow rate of 50 mL min⁻¹ to clean the surface of the photocatalyst. The adsorption equilibrium state was used as the background for subtraction, and the mixed gas was flowed for 15 minutes. After reaching adsorption equilibrium, the intermediate species formed during the reaction were monitored online using an LED light source.

Section 4: Results and discussion

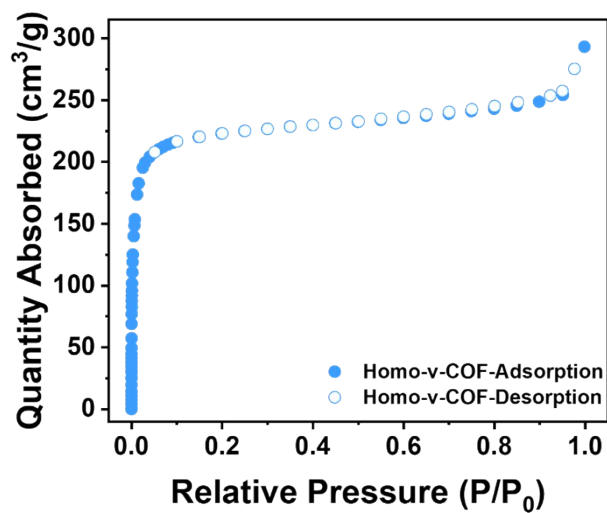


Figure S1 Nitrogen adsorption and desorption isotherms of Homo-v-COF.

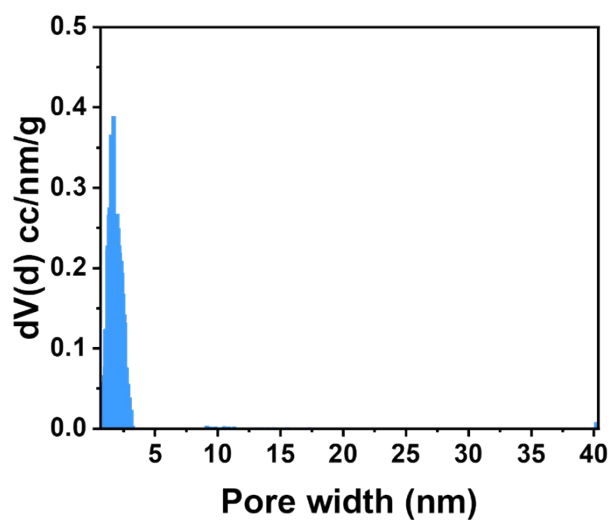


Figure S2 Pore size distribution of Homo-v-COF calculated by NLDFT model.

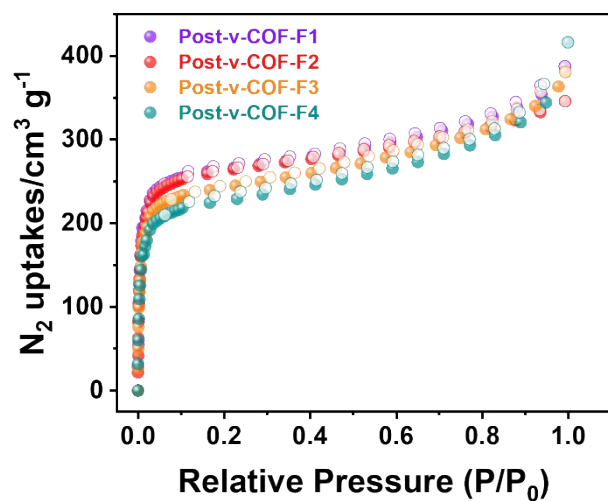


Figure S3 Nitrogen adsorption and desorption isotherms of Post-v-COF-Fx.

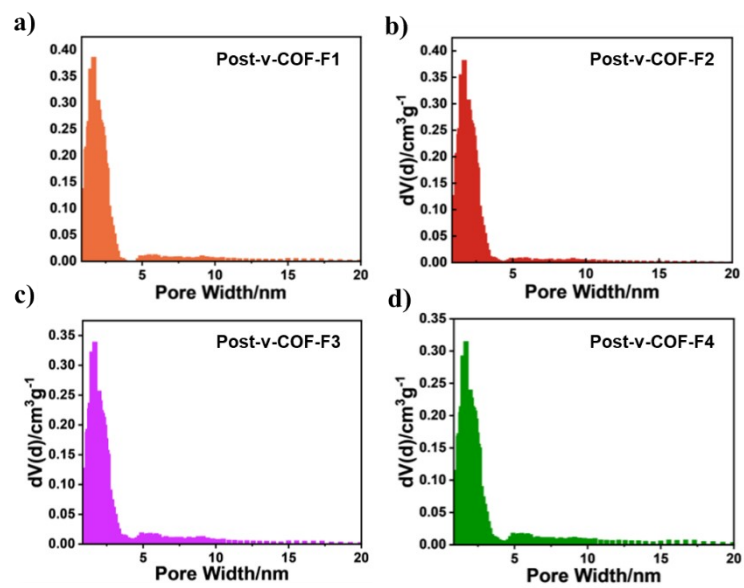


Figure S4 Pore size distribution of Post-v-COF-Fx calculated by NLDFT model.

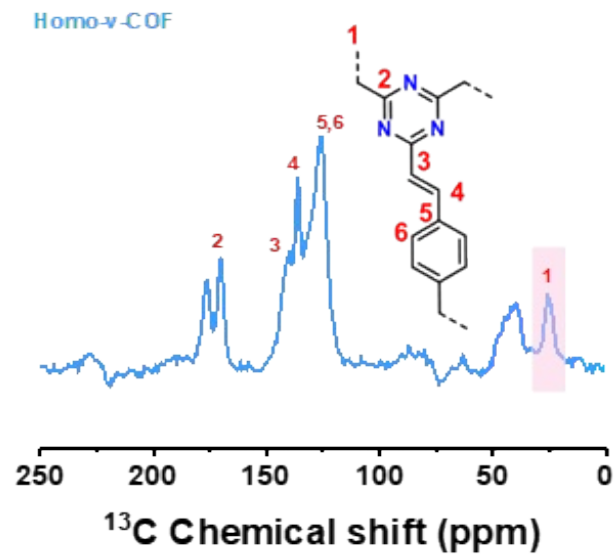


Figure S5 ^{13}C CP/MAS solid-state NMR spectra of Homo-v-COF.

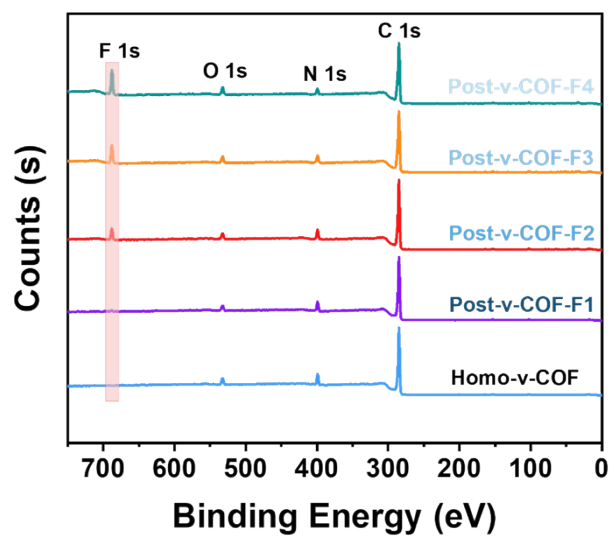


Figure S6 High resolution XPS spectra of Homo-v-COF and Post-v-COF-Fx.

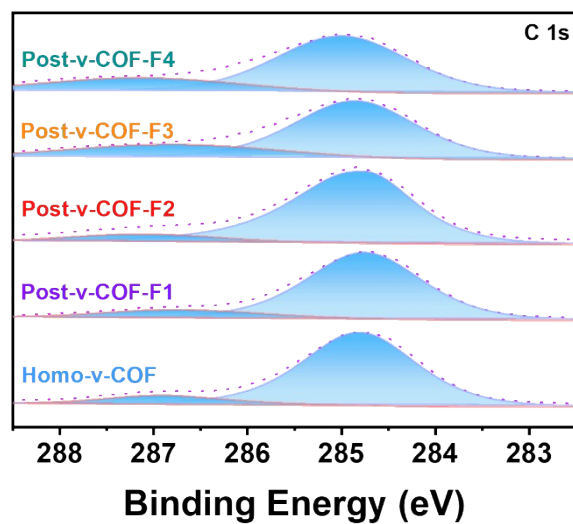


Figure S7 High-resolution XPS C 1s spectra of Homo-v-COF and Post-v-COF-Fx.

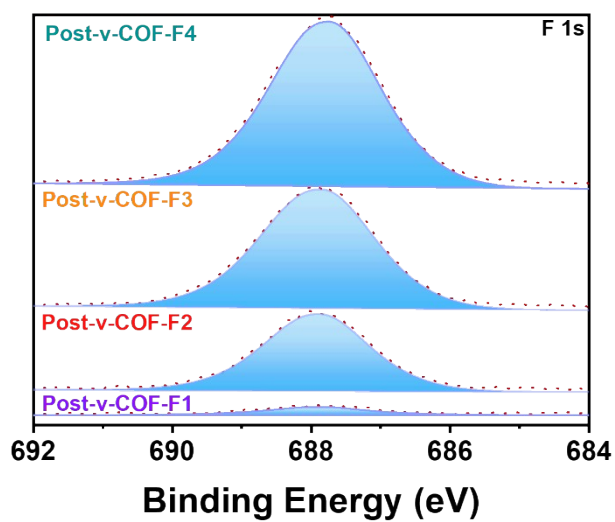


Figure S8 High-resolution XPS F 1s spectrum of Post-v-COF-Fx.

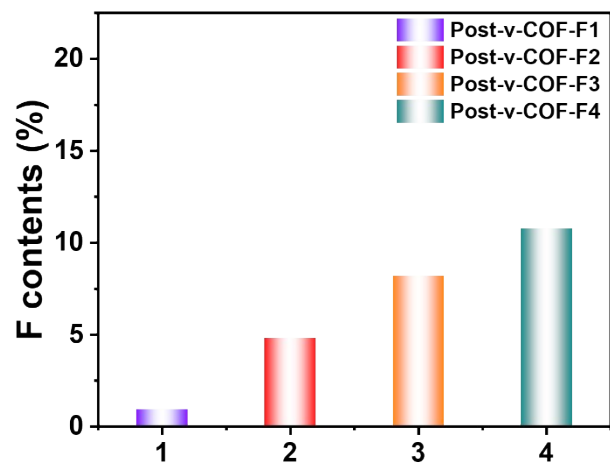


Figure S9 Fluorine contents of Post-v-COF-Fx determined by High resolution XPS.

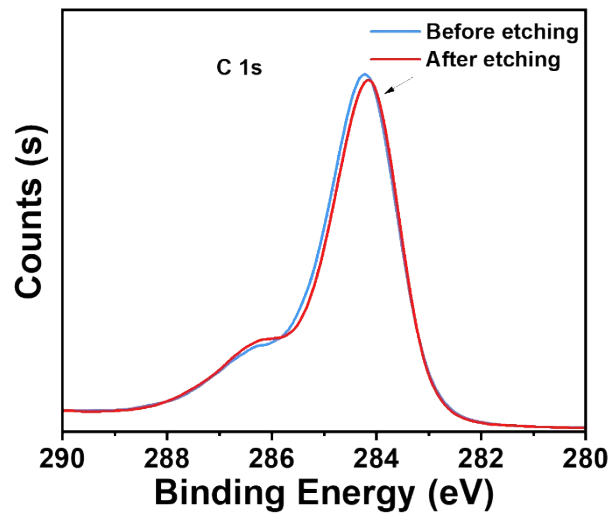


Figure S10 XPS depth profiling of Post-v-COF-F2 by etching method.

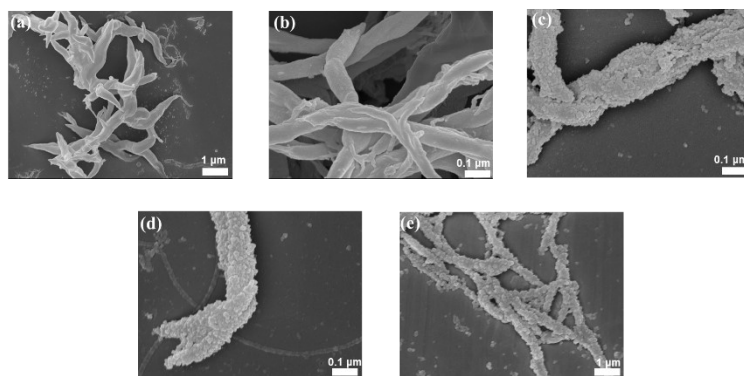


Figure S11 SEM images of Homo-v-COF and Post-v-COF-Fx.

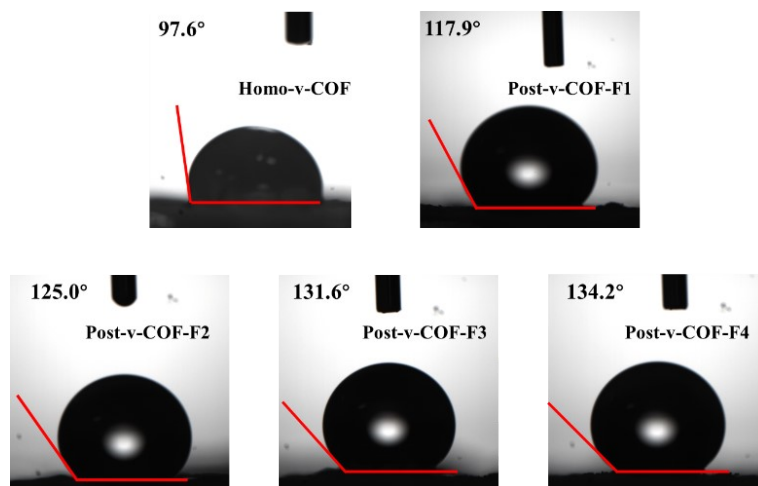


Figure S12 Water contact angle characterization of HOMO-v-COF and Post-v-COF-Fx.

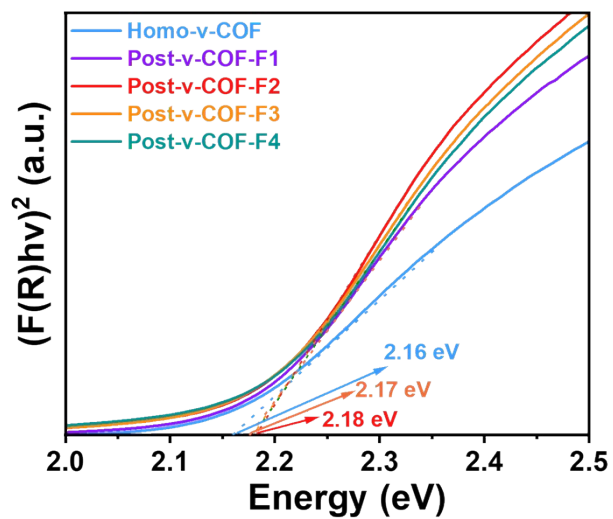


Figure S13 Optical band gaps of Homo-v-COF and Post-v-COF-Fx.

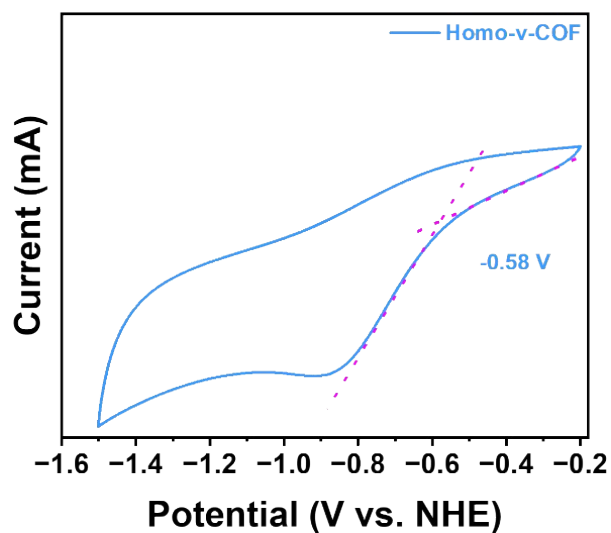


Figure S14 Cyclic voltammetry curves of Homo-v-COF.

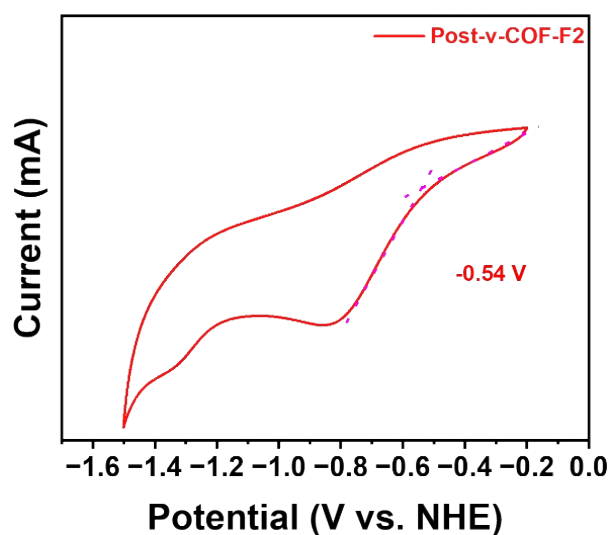


Figure S15 Cyclic voltammetry curves of Post-v-COF-F2.

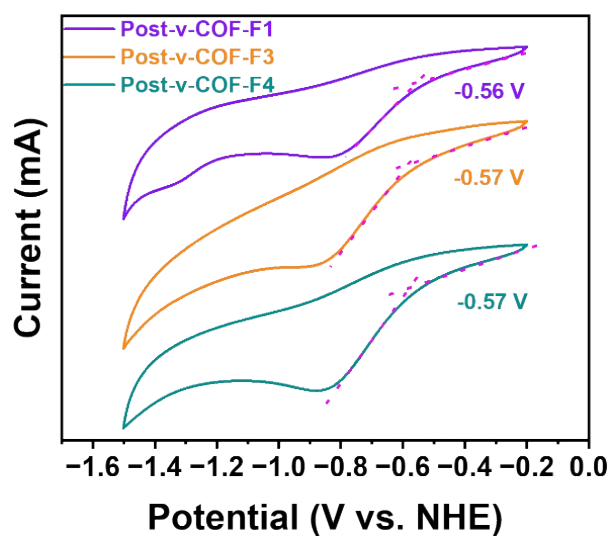


Figure S16 Cyclic voltammetry curves of Post-v-COF-Fx.

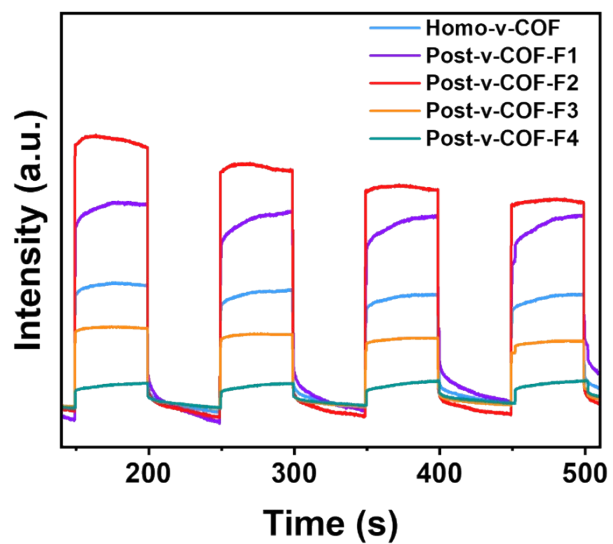


Figure S17 Transient photocurrent measurements of Homo-v-COF and Post-v-COF-Fx.

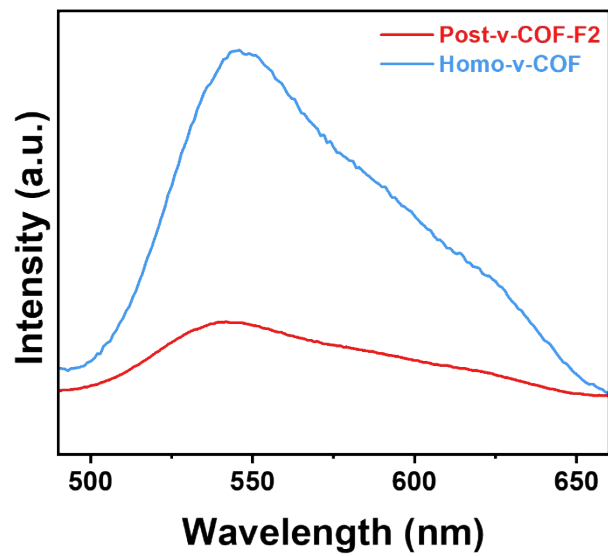


Figure S18 Photoluminescence spectra of Homo-v-COF and Post-v-COF-F2.

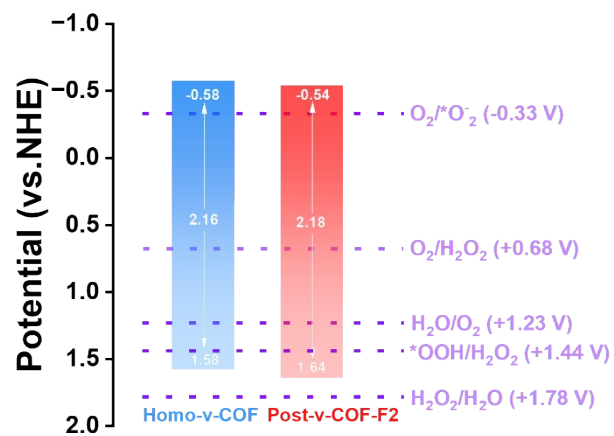


Figure S19 Band alignment of the Homo-v-COF and Post-v-COF-F2.

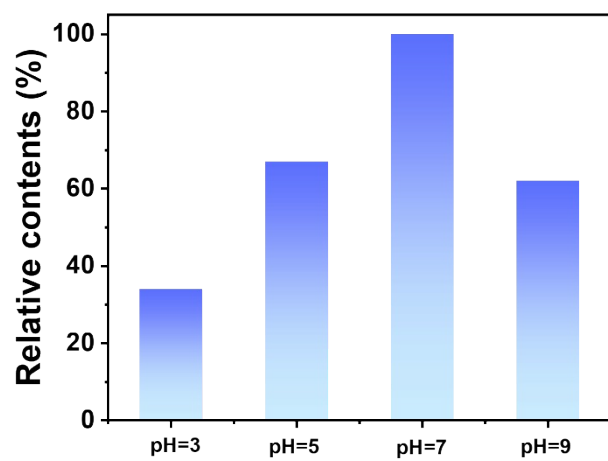


Figure S20 Photocatalytic H₂O₂ performance of Post-v-COF-F2 under varying pH conditions.

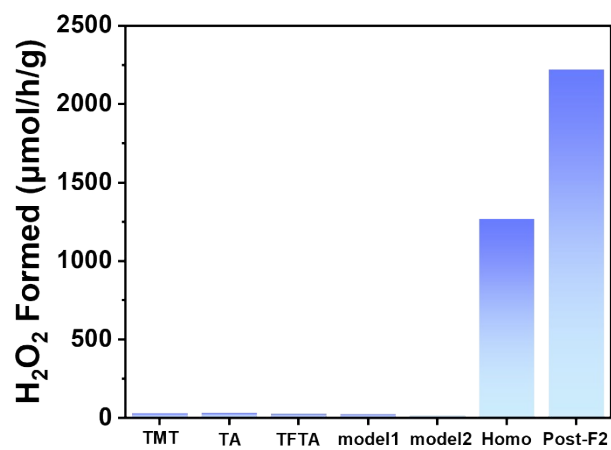


Figure S21 Comparison of photocatalytic H₂O₂ production performance of monomer (TMT, TA, TFTA), model compounds, Homo-v-COF and Post-v-COF-F2.

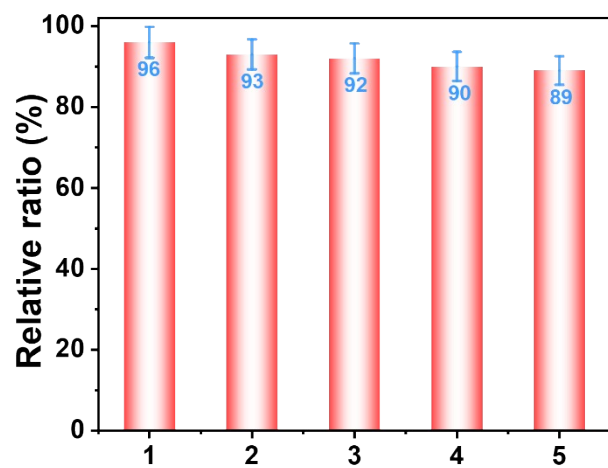


Figure S22 Catalytic reaction cycling performance test of Post-v-COF-F2.

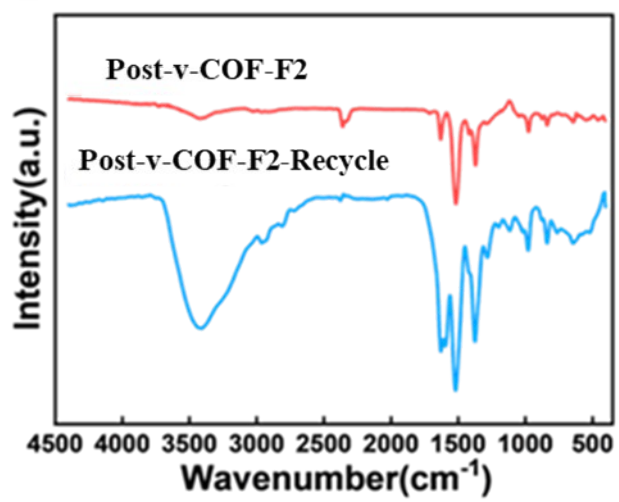


Figure S23 FTIR spectrum of Post-v-COF-F2 after four photocatalytic cycles.

Table S1: Summary of the performance of recently reported organic materials for photocatalytic production of H₂O₂.

Photocatalysts	Reaction Condition	Solvent	H ₂ O ₂ (μmol/h/g)	Ref
Homo-v-COF	λ=455 nm LED blue light	H₂O	1267	This work
Post-v-COF-F2	λ=455 nm LED blue light	H₂O	2219	This work
OCN-500	λ>420 nm	H ₂ O	106	5
ZnPPc-g-C ₃ N ₄	\	\	114	6
C ₅ N ₂	λ>420 nm	H ₂ O	698	7
PEI/C ₃ N ₄	λ>420 nm	H ₂ O	208	8
CTF-BDDBN	λ>420 nm	H ₂ O	97.2	9
TAPD-(Me) ₂ COF	λ>420 nm	H ₂ O: EtOH=9:1	97	10
SonoCOF-F2	λ>420 nm	H ₂ O	164	11
TAPQ-COF-12	λ>420 nm	H ₂ O	420	12
TiCOF-spn	\	\	489.94	13
COF-TfpBpy	λ > 420 nm	H ₂ O	695	14
TDB-COF	λ>420 nm	H ₂ O	723.5	15
COF-must-8	λ>420 nm	H ₂ O : EtOH=9:1	1081	16
COF-TAPB-BPDA	λ>420 nm	H ₂ O : BA=4:1	1240	17
Py-Da-COF	λ>420 nm	H ₂ O : BA=9:1	1242	18
TPB-DMTP-COF	λ>420 nm	H ₂ O	1565	19
DETH-COF	λ=450 nm	H ₂ O	1665	20
TF ₅₀ -COF	λ>400 nm	H ₂ O : EtOH=9:1	1739	21
HEP-TAPT-COF	λ > 420 nm	H ₂ O	1750	22
EBA-COF	λ=420 nm	H ₂ O : EtOH=9:1	1830	23

CoPc-BTM-COF	$\lambda > 400$ nm	H ₂ O : EtOH=9:1	2096	24
TAPB-PDA-OH	$\lambda = 420$ nm	H ₂ O : EtOH=9:1	2117.6	25
sp ² c-CTF-4@AB	$\lambda > 420$ nm	H ₂ O	2758	26
TPB-DMTP-COF	$\lambda > 420$ nm	H ₂ O	2882	27
Bpt-CTF	350-780 nm	H ₂ O	3268.1	28
FS-COFs	$\lambda > 420$ nm	H ₂ O	3904	29
TAH-COF	$\lambda > 420$ nm	H ₂ O	6003	30

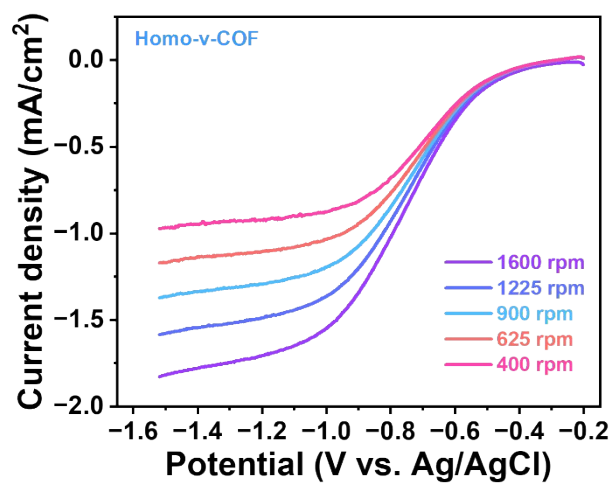


Figure S24 Rotating disc electrode test of Homo-v-COF.

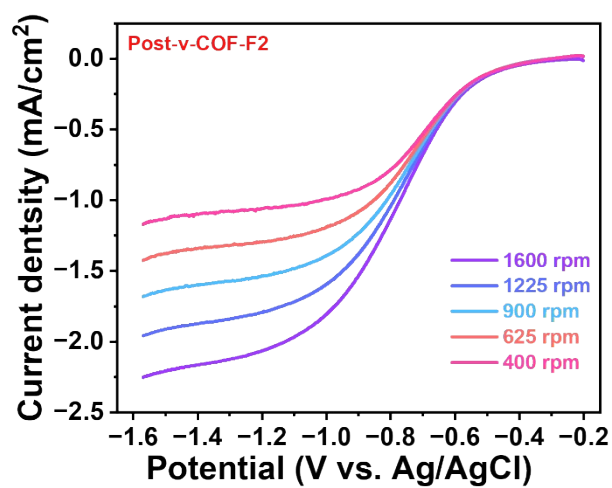


Figure S25 Rotating disc electrode test of Post-v-COF-F2.

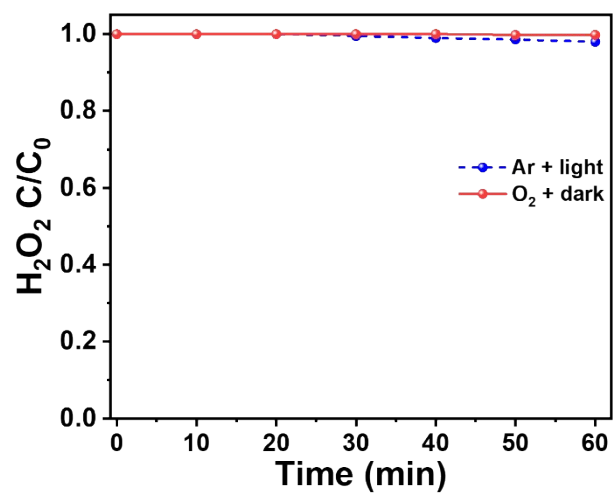
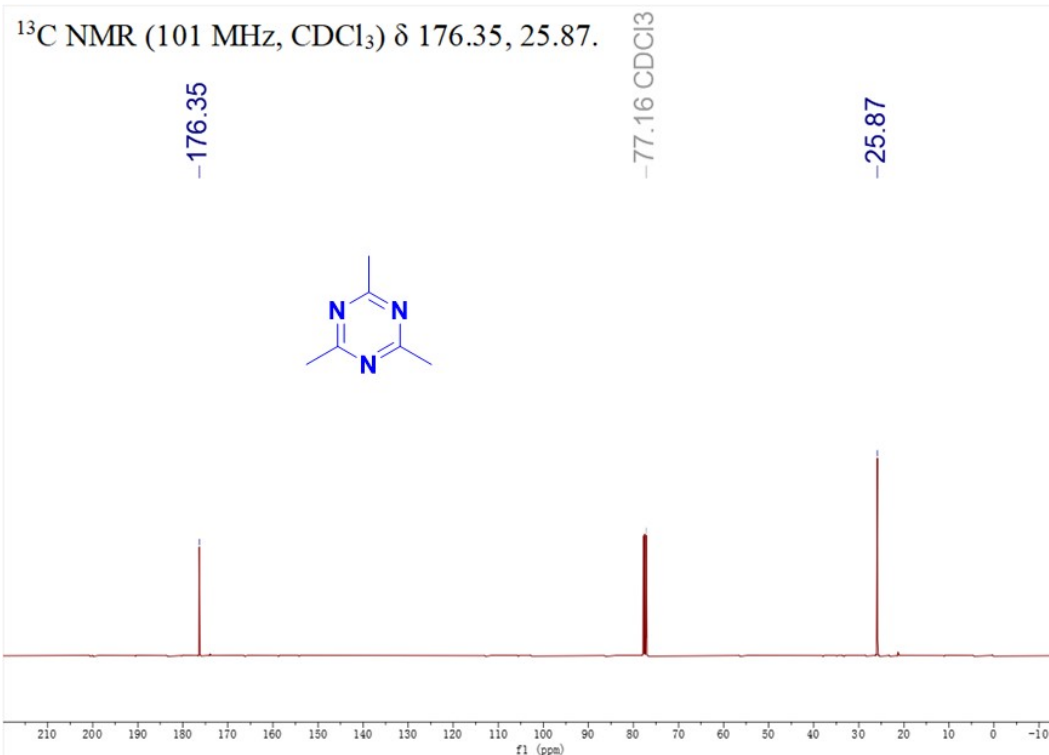
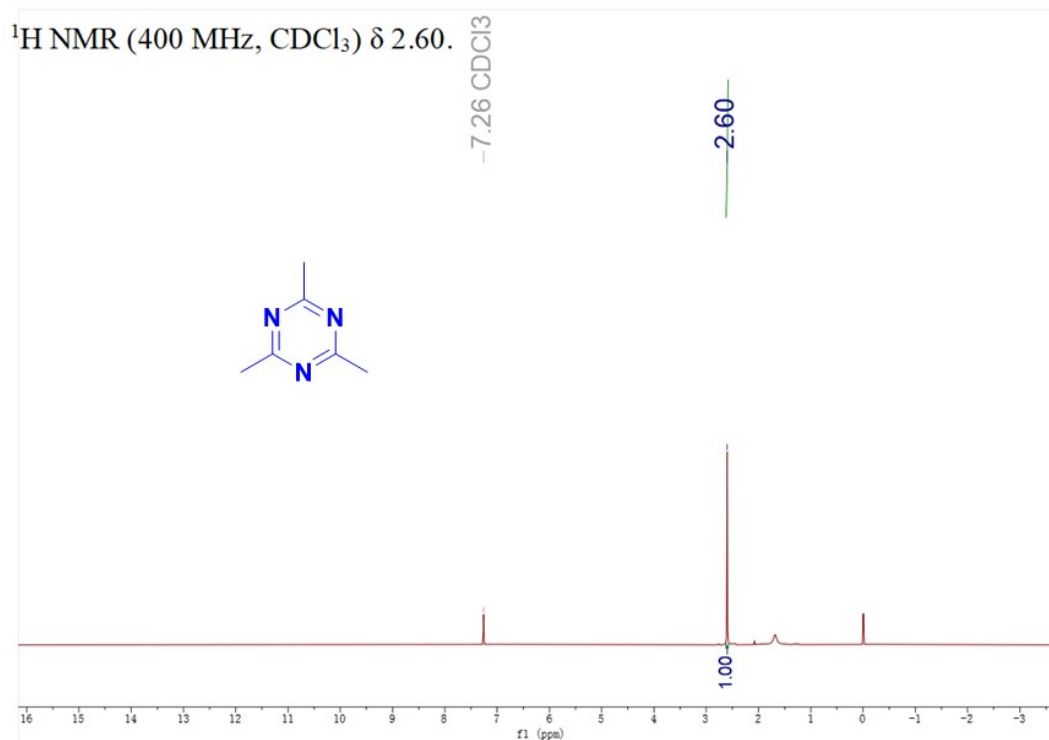


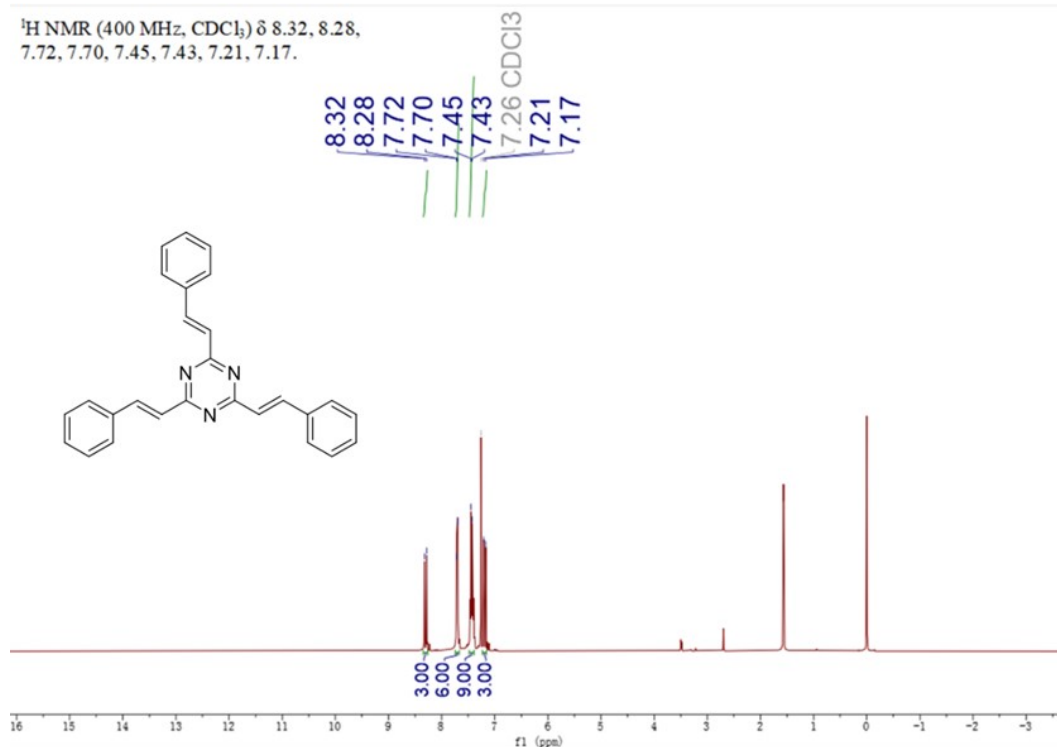
Figure S26 Time-dependent profiles of photocatalytic H_2O_2 decomposition rate of Post-v-COF-F2 under Ar conditions or dark conditions.

Section 5: NMR Spectra of monomers



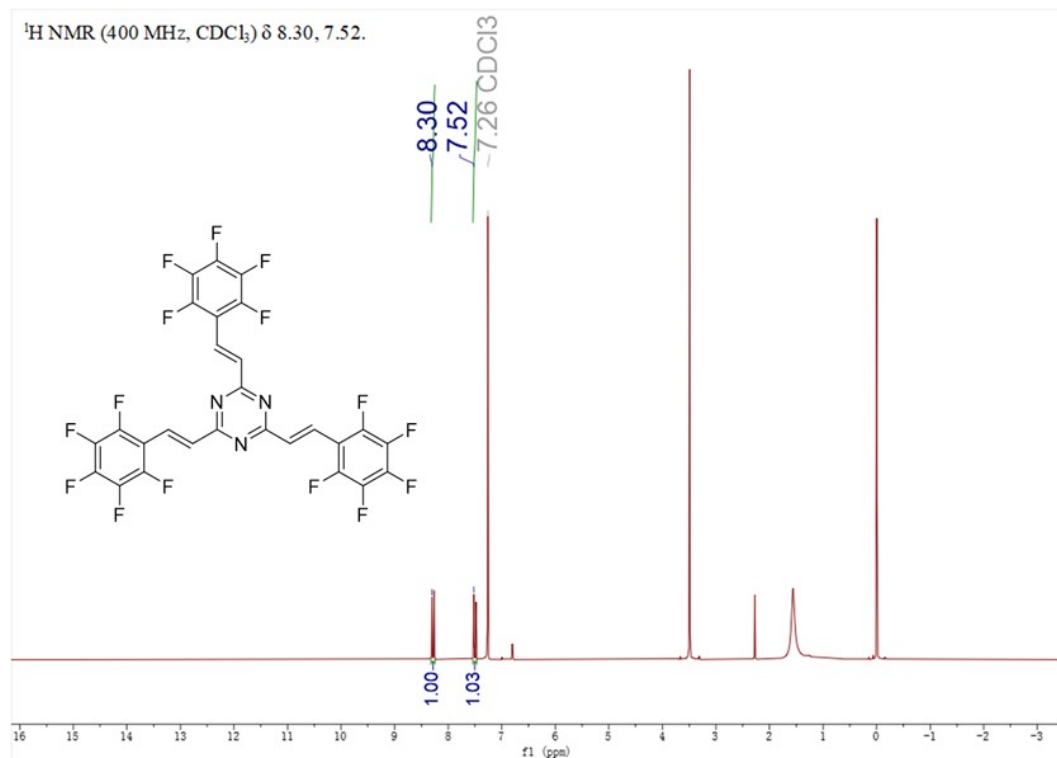
The ^1H -NMR and ^{13}C -NMR spectra of TMT

^1H NMR (400 MHz, CDCl_3) δ 8.32, 8.28, 7.72, 7.70, 7.45, 7.43, 7.21, 7.17.



The ^1H -NMR spectra of model compound 1

^1H NMR (400 MHz, CDCl_3) δ 8.30, 7.52.



The ^1H -NMR spectra of model compound 2

Reference:

- 1 S. Wei, F. Zhang, W. Zhang, P. Qiang, K. Yu, X. Fu, D. Wu, S. Bi and F. Zhang, *J. Am. Chem. Soc.*, 2019, **141**, 14272.
- 2 A. Acharjya, P. Pachfule, J. Roeser, F. Schmitt and A. Thomas, *Angew Chem Int Ed.*, 2019, **58**, 14865.
- 3 J. Chen, N. Sun, Q. Gao and W. Wei. *Chemical Industry and Engineering Progress.*, 2021, **40**, 6765.
- 4 C. Su, M. Acik, K. Takai, J. Lu, S. Hao, Y. Zheng, P. Wu, Q. Bao, T. Enoki, Y. J. Chabal and K. Ping Loh, *Nat Commun.*, 2012, **3**, 1298.
- 5 Z. Wei, M. Liu, Z. Zhang, W. Yao, H. Tan and Y. Zhu, *Energy Environ. Sci.*, 2018, **11**, 2581.
- 6 Y. Ye, J. Pan, F. Xie, L. Gong, S. Huang, Z. Ke, F. Zhu, J. Xu and G. Ouyang, *Proc. Natl. Acad. Sci. U.S.A.*, 2021, **118**, e2103964118.
- 7 J. Ma, X. Peng, Z. Zhou, H. Yang, K. Wu, Z. Fang, D. Han, Y. Fang, S. Liu, Y. Shen and Y. Zhang, *Angew Chem Int Ed.*, 2022, **61**, e202210856.
- 8 X. Zeng, Y. Liu, Y. Kang, Q. Li, Y. Xia, Y. Zhu, H. Hou, M. H. Uddin, T. R. Gengenbach, D. Xia, C. Sun, D. T. McCarthy, A. Deletic, J. Yu and X. Zhang, *ACS Catal.*, 2020, **10**, 3697.
- 9 L. Chen, L. Wang, Y. Wan, Y. Zhang, Z. Qi, X. Wu and H. Xu, *Advanced Materials.*, 2020, **32**, 1904433.
- 10 C. Krishnaraj, H. Sekhar Jena, L. Bourda, A. Laemont, P. Pachfule, J. Roeser, C. V. Chandran, S. Borgmans, S. M. J. Rogge, K. Leus, C. V. Stevens, J. A. Martens, V. Van Speybroeck, E. Breynaert, A. Thomas and P. Van Der Voort, *J. Am. Chem. Soc.*, 2020, **142**, 20107.
- 11 W. Zhao, P. Yan, B. Li, M. Bahri, L. Liu, X. Zhou, R. Clowes, N. D. Browning, Y. Wu, J. W. Ward and A. I. Cooper, *J. Am. Chem. Soc.*, 2022, **144**, 9902.
- 12 X. Zhang, J. Zhang, J. Miao, X. Wen, C. Chen, B. Zhou and M. Long, *Chemical Engineering Journal.*, 2023, **466**, 143085.
- 13 W. Han, H. Lu, J. Fu, X. Liu, X. Zhu, X. Yan, J. Zhang, Y. Jiang, H. Dong and Z. Gu, *Chemical Engineering Journal.*, 2022, **449**, 137802.
- 14 M. Kou, Y. Wang, Y. Xu, L. Ye, Y. Huang, B. Jia, H. Li, J. Ren, Y. Deng, J. Chen, Y. Zhou, K. Lei, L. Wang, W. Liu, H. Huang and T. Ma, *Angew Chem Int Ed.*, 2022, **61**, e202200413.
- 15 Z. Zhou, M. Sun, Y. Zhu, P. Li, Y. Zhang, M. Wang and Y. Shen, *Applied Catalysis B: Environmental.*, 2023, **334**, 122862.
- 16 M. Wu, Z. Shan, J. Wang, T. Liu and G. Zhang, *Chemical Engineering Journal.*, 2023, **454**, 140121.
- 17 T. Yang, Y. Chen, Y. Wang, X. Peng and A. Kong, *ACS Appl. Mater. Interfaces*, 2023, **15**, 8066.
- 18 J. Sun, H. Sekhar Jena, C. Krishnaraj, K. Singh Rawat, S. Abednatanzi, J. Chakraborty, A. Laemont, W. Liu, H. Chen, Y. Liu, K. Leus, H. Vrielinck, V. Van Speybroeck and P. Van Der Voort, *Angew Chem Int Ed.*, 2023, **62**, e202216719.
- 19 L. Li, L. Xu, Z. Hu and J. Yu, *Adv Funct Materials.*, 2021, **31**, 2106120.
- 20 G. Pan, X. Hou, Z. Liu, C. Yang, J. Long, G. Huang, J. Bi, Y. Yu and L. Li, *ACS Catal.*, 2022, **12**, 14911.
- 21 H. Wang, C. Yang, F. Chen, G. Zheng and Q. Han, *Angew Chem Int Ed.*, 2022, **61**, e202202328.
- 22 D. Chen, W. Chen, Y. Wu, L. Wang, X. Wu, H. Xu and L. Chen, *Angew Chem Int Ed.*, 2023, **62**, e202217479.
- 23 L. Zhai, Z. Xie, C. Cui, X. Yang, Q. Xu, X. Ke, M. Liu, L. Qu, X. Chen and L. Mi, *Chem. Mater.*, 2022, **34**, 5232.
- 24 Q. Zhi, W. Liu, R. Jiang, X. Zhan, Y. Jin, X. Chen, X. Yang, K. Wang, W. Cao, D. Qi and J. Jiang, *J. Am. Chem. Soc.*, 2022, **144**, 21328.
- 25 Y. Yang, J. Kang, Y. Li, J. Liang, J. Liang, L. Jiang, D. Chen, J. He, Y. Chen and J. Wang, *New J. Chem.*, 2022, **46**, 21605.
- 26 Q. Xie, A. Chen, X. Li, C. Xu, S. Bi, W. Zhang, J. Tang, C. Pan, F. Zhang and G. Yu, *Chem. Sci.*, 2025, **16**, 2215.
- 27 L. Li, L. Xu, Z. Hu and J. C. Yu, *Adv Funct Materials.*, 2021, **31**, 2106120.
- 28 C. Wu, Z. Teng, C. Yang, F. Chen, H. B. Yang, L. Wang, H. Xu, B. Liu, G. Zheng and Q. Han, *Advanced Materials.*, 2022, **34**, 2110266.
- 29 Y. Luo, B. Zhang, C. Liu, D. Xia, X. Ou, Y. Cai, Y. Zhou, J. Jiang and B. Han, *Angew Chem*

Int Ed., 2023, **62**, e202305355.

30 T. Xu, Z. Wang, W. Zhang, S. An, L. Wei, S. Guo, Y. Huang, S. Jiang, M. Zhu, Y. Zhang and W. Zhu, *J. Am. Chem. Soc.*, 2024, **146**, 20107.